Classification and Identification of Buckling Modes of Steel Columns under Cyclic Loading

Gulen Ozkula, M.ASCE[1]; and Chia-Ming Uang, M.ASCE[2]

Abstract: Wide-flange columns are commonly used for the construction of special moment frames and braced frames. For special moment frames, design engineers routinely use deep sections to meet the stringent code-specified story drift limits in order to achieve economy in recent years. Columns with shallow and stocky sections are common for braced frame construction. Observation made from two recent experimental studies involving both deep and shallow columns under axial compression and cyclic drifts showed a variety of buckling modes. A classification with three cyclic buckling modes is proposed in this paper; subsets of each buckling mode are also presented. A parameter measuring the relative rotational restraint that the web provides to each flange is derived. After calibrating this parameter with the test results, a practical procedure that can predict the governing cyclic buckling mode is proposed. **DOI: [10.1061/JSENDH. STENG-12156](https://doi.org/10.1061/JSENDH.STENG-12156).** © 2023 American Society of Civil Engineers.

Author keywords: Steel beam-column; Local buckling; Lateral-torsional buckling; Slenderness ratios; Hysteretic behavior; Cyclic loading.

Introduction

Before the 1994 Northridge, California earthquake, shallow wide-flange columns (e.g., W12 or W14) were more commonly used in ductile moment-resisting frames because of their comparable strong- and weak-axis radii of gyration. However, it was challenging to continue to design columns using shallow sections since the lateral flexibility feature of moment frames requires a large moment of inertia in the plane of the frames to satisfy the code-enforced story drift requirement (ASCE 2016). Instead, engineers turned to deeper steel columns. For example, Fig. 1 shows one shallow and one deep section with the same strong-axis moment of inertia. The benefit of using the deep W27 × 258 section is obvious; the weight of the column is reduced from 900 to 384 kg/m (605 to 258 lb/ft). But the width-to-thickness ratios for both flange local buckling (FLB) and web local buckling (WLB) checks are much larger for the deep section. Because the radius of gyration about the weak-axis (r_y) is smaller, the deep column is also prone to out-of-plane, global-type buckling like flexural buckling (FB) or lateral-torsional buckling (LTB). The three slenderness parameters are defined as follows:

$$\text{FLB: } \lambda_f = \frac{b_f}{2t_f} \tag{1a}$$

$$\text{WLB: } \lambda_w = \frac{h}{t_w} \tag{1b}$$

$$\text{LTB or FB: } \lambda_L = \frac{L}{r_y} \tag{1c}$$

where b_f, t_f, h, and t_w are defined in Fig. 1, and L is the column length. Although both sections in Fig. 1 satisfy the highly ductile section requirements per AISC 341 (AISC 2016a), the three slenderness parameters for both local and global buckling checks for the deeper column are much larger.

For applications in braced frames, Newell and Uang (2008) conducted an AISC-sponsored research project which involved full-scale testing of W14 columns (W14 × 132 to W14 × 370) subjected to various levels of axial load and cyclic drifts. The ranges of the slenderness parameters for these nine specimens were $3.1 \leq \lambda_f \leq 7.1$, $6.9 \leq \lambda_w \leq 17.7$, and $42.2 \leq \lambda_L \leq 47.9$. It was concluded that this type of shallow columns, which had a d/b_f ratio of about 1.1, had a ductility capacity much higher than that specified in ASCE 41 (ASCE 2017) even under high axial load. These large deformation capacities were, in part, achieved due to the delay in FLB resulting from the stabilizing effect provided by the stocky web with a low λ_w value. But finite element simulation of W27 columns conducted by Newell and Uang (2008) showed that the cyclic behavior of deep columns can experience a rapid flexural strength degradation due to significant flange and web buckling.

According to AISC 341 (AISC 2016a), columns in special moment frames shall be designed to satisfy the strong column-weak beam requirement, but flexural yielding of columns at the base is permitted. Therefore, researchers started to pay attention to the deep column behavior and design for applications in moment frames about a decade ago (e.g., Elkady and Lignos 2012; Zargar et al. 2014; Elkady and Lignos 2015; Fogarty and El-Tawil 2016; Fogarty et al. 2017; Ozkula et al. 2017; Elkady and Lignos 2018; Wu et al. 2018; Cravero et al. 2020). The National Institute of Standards and Technology (NIST) also developed a comprehensive research plan to study this type of columns at the member, subassemblage, and system levels (NIST 2011). Research at the member level, which started in 2013, was conducted at the University of California, San Diego (UCSD), and the test results are summarized in Chansuk et al. (2021). Based on these full-scale test results and the associated finite element simulation (Ozkula and Uang 2015),

[1]Assistant Professor, Dept. of Civil and Environmental Engineering, Univ. of Wisconsin-Platteville, Platteville, WI 53818. ORCID: https://orcid.org/0000-0002-1947-6362. Email: ozkulag@uwplatt.edu

[2]Professor, Dept. of Structural Engineering, Univ. of California San Diego, La Jolla, CA 92093 (corresponding author). ORCID: https://orcid.org/0000-0002-8467-9748. Email: cmu@ucsd.edu
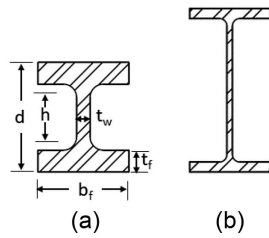
Fig. 1. Shallow versus deep wide-flange shapes: (a) W14 × 605; and (b) W27 × 258.

limiting λ_w ratios for highly ductile and moderately ductile sections, i.e., λ_{hd} and λ_{md} for special moment frames (SMF) and intermediate moment frames (IMF) per AISC 341, have been proposed (Ozkula et al. 2021).

Objective and Scope

It was observed from both the previously-mentioned AISC- and NIST-sponsored test programs that the failure modes between shallow and deep columns are very different. For deep columns, interactive local buckling involving both flange and the web would

occur. Depending on the λ_f and λ_w values, some columns also experienced out-of-plane buckling. The objective of this paper is first to classify buckling modes (both local and global) observed from both test programs, which is then followed by the development of a practical method to predict the governing buckling mode of wide-flange columns under axial compression and cyclic drifts.

NIST Testing Program

Table 1 shows 35 wide-flange columns (W30, W24, W18, and W14 sections) that were part of those tested in the NIST research program (Chansuk et al. 2021). The overall geometry of the test setup is shown in Fig. 2. Specimens were tested in a horizontal position with one end attached to a strong wall fixture, while the other end was attached to a reaction block on the shake table. Each specimen was 5,486 mm long with 76 mm-thick base plates welded at each end. A992 steel was specified for the specimens. The section and member slenderness ratios of these columns fall in the following ranges:

$$4.81 \leq \lambda_f \leq 6.94, 28.7 \leq \lambda_w \leq 54.6, \text{ and } 71.1 \leq \lambda_L \leq 161.2 \quad (2)$$

For axial load application, letter L, M, or H in the specimen designation represents low ($C_a = 0.2$), medium ($C_a = 0.4$), and

Table 1. Test matrix

Group No.	Shape	Specimen designation	Slenderness rations			Column axial load	Buckling mode	$\dfrac{L_r}{r_y}$
			λ_f	λ_w	λ_L	C_a		
1	W24 × 176	1L	4.81	28.7	71.1	0.2	CB	142
		1M				0.4		
		1H				0.6		
2	W24 × 131	2Z	6.7	35.6	72.7	0	ALB	127
		2L				0.2		
		2L-P				0.2		
		2M				0.4		
		2M-NF				0.4		
		2H				0.6		
3	W24 × 104	3L	8.5	43.1	74.2	0.2	ALB	118
		3M				0.4		
		3H				0.6		
4	W24 × 84	4L	5.86	45.9	110.8	0.2	CB	123
		4M				0.4		
5	W24 × 55	5L	6.94	54.6	161.2	0.2	Elastic LTB	119
		5LM				0.3		
		5M				0.4		
11	W24 × 176	11M	4.81	28.7	71.05	0.4	CB	143
		11H-VAM				0.6		
		11H-BC				0.6		
12	W30 × 261	12LM	4.59	28.7	61.19	0.3	CB	138
		12LM-P				0.3		
13	W30 × 173	13M	7.04	40.8	63.16	0.4	ALB	114
		13M-BC				0.4		
14	W30 × 90	14L	8.52	57.5	103.35	0.2	ALB	110
15	W18 × 192	15L	3.27	16.7	77.42	0.2	CB	200
16	W18 × 130	16M	4.65	23.9	80.0	0.4	CB	163
		16M-BC				0.4		157
17	W18 × 76	17L	8.11	37.8	82.76	0.4	ALB	114
21	W18 × 130	21M-NF	4.65	23.9	80.0	0.4	CB	151
22	W30 × 148	22L	4.44	41.6	94.7	0.2	CB	124
23	W18 × 60	23L	5.44	38.7	100.0	0.2	CB	131
24	W14 × 82	24L	5.92	22.4	67.7	0.2	ALB	156
25	W14 × 53	25L	6.11	30.9	87.5	0.2	CB	130
26	W14 × 132	26LM	7.15	17.7	44.7	0.3	ALB	174
		26LM-VAM				0 to 0.6		164

Fig. 2. Test setup.

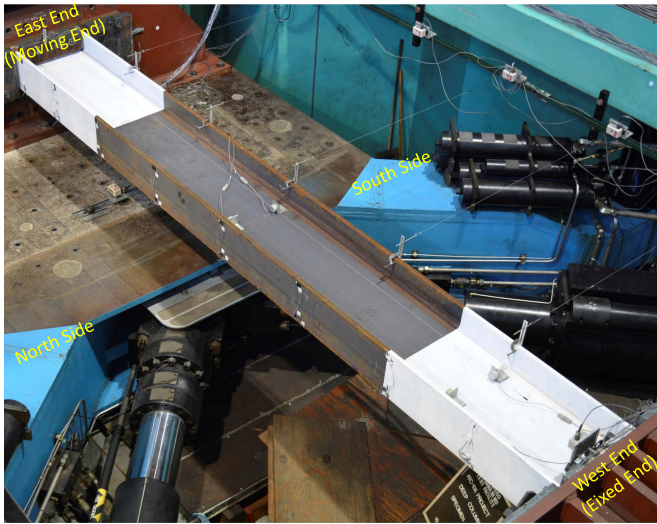**Fig. 3.** Distribution of deep column specimens in the $\lambda_f - \lambda_w$ domain.

high ($C_a = 0.6$) axial load level, respectively, with C_a defined per the 2010 edition of AISC 341:

$$C_a = \frac{P_u}{\phi_c A_g F_y} \tag{3}$$

where P_u = applied axial force; A_g = cross-sectional area; F_y = specified minimum yield stress; and $\phi_c = 0.9$. Five specimens (5LM, 12LM, 12LM-P, 26LM, 26LM-VAM) with a designation LM had $C_a = 0.3$. Only one specimen (2Z) was tested without an axial load, i.e., it was tested cyclically as a flexural beam. The axial load was maintained constant for all except two specimens (11H-VA and 26LM-VAM), where the varying axial load simulating the effect of overturning moment on the exterior columns of a frame was applied.

Per Section K2.4b of AISC 341 for prequalified beam-to-column moment connection testing, the cyclic story drift loading sequence of increasing amplitudes was used for all except two specimens; the latter (2L-P, 12LM-P) were tested monotonically for comparison with their cyclic counterparts. All specimens listed in Table 1 were tested for strong-axis, reverse-curvature bending. The fixed-fixed boundary condition was used for most of the specimens, with four specimens (11H-BC, 13M-BC, 16M-BC, and 21M-VAU-BC) tested with a fixed-rotating boundary condition to simulate the rotational flexibility at the top end of the first-story columns (Chansuk et al. 2021).

Fig. 3 depicts the distribution of specimens based on the flange and web slenderness ratios. For FLB, both λ_{hd} and λ_{md} as specified in AISC 341 for highly ductile and moderately ductile members are shown. Values of λ_{hd} for WLB at three normalized axial force levels are also shown. The figure shows that most of the specimens had highly ductile sections that met the requirement for SMF. Testing showed that one column (W24 × 55) that had the highest λ_L (= 161.2) experienced LTB in the elastic range and, thus, this specimen is excluded in the following discussion. All the other specimens were deformed into the inelastic range.

The failure modes observed from the NIST test program for deeper columns varied significantly among the specimens. The observed cyclic response and buckling mode were also very different from those observed from the W14 columns tested in the AISC test program (Newell and Uang 2008). To illustrate the difference, refer to Fig. 4 for a comparison of the sample responses of three
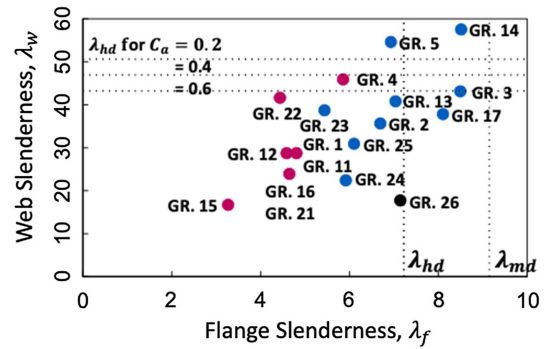
specimens with a comparable axial force level. The abscissa is the story drift angle (*SDA*) and the ordinate is the member end moment normalized by the reduced plastic moment, M_{pc}:

$$M_{pc} = M_p = F_y Z_x \quad \text{when } P_u/P_y < 0.15 \tag{4a}$$

$$M_{pc} = 1.18(1 - P_u/P_y)M_p \quad \text{when } P_u/P_y \geq 0.15 \tag{4b}$$

Fig. 4(a) shows that the W14 × 176 shallow-column specimen provided a stable hysteretic response up to a *SDA* of 0.1 rad. But two deep-column specimens (W24 × 131 and W24 × 176) had a much lower drift capacity with a significant degradation in lateral strength. It will be shown later that these two specimens also experienced different buckling modes. Furthermore, Fig. 4(b) shows that the two deep column specimens had a significant axial shortening due to buckling, an undesirable behavior that the shallow column specimen did not have. A comparison of the backbone curves in Fig. 4(c) clearly shows that there is a need to identify the governing buckling mode before meaningful modeling of wide-flange columns can be made. Several buckling modes were observed from the NIST and AISC test programs, and the observed deformations could be confusing at times. In the following, a classification of cyclic buckling modes is first presented. A practical procedure is then presented to predict the governing buckling mode.

In the NIST test program it was observed that the effects of axial force level, axial loading type (constant or varying that reflects the overturning effect of the frame), lateral loading type (symmetric-type loading of increasing amplitude or near-fault type loading) and the boundary condition (fixed-fixed or fixed-rotating) did not change the governing buckling mode; see Chansuk et al. (2021) for details.

Observed Column Buckling Modes

The governing buckling modes observed from both test programs can be grouped into three types, which are defined as symmetric flange buckling (SFB), antisymmetric local buckling (ALB), and coupled buckling (CB) herein.

Symmetric Flange Buckling Mode

SFB occurs in wide-flange columns with a highly ductile section featuring low flange and web slenderness ratios i.e., mostly shallow columns like W10 to W14 shapes. This buckling pattern occurs when the column in reverse curvature develops plastic hinges at member ends. The deformation of the column under strong-axis
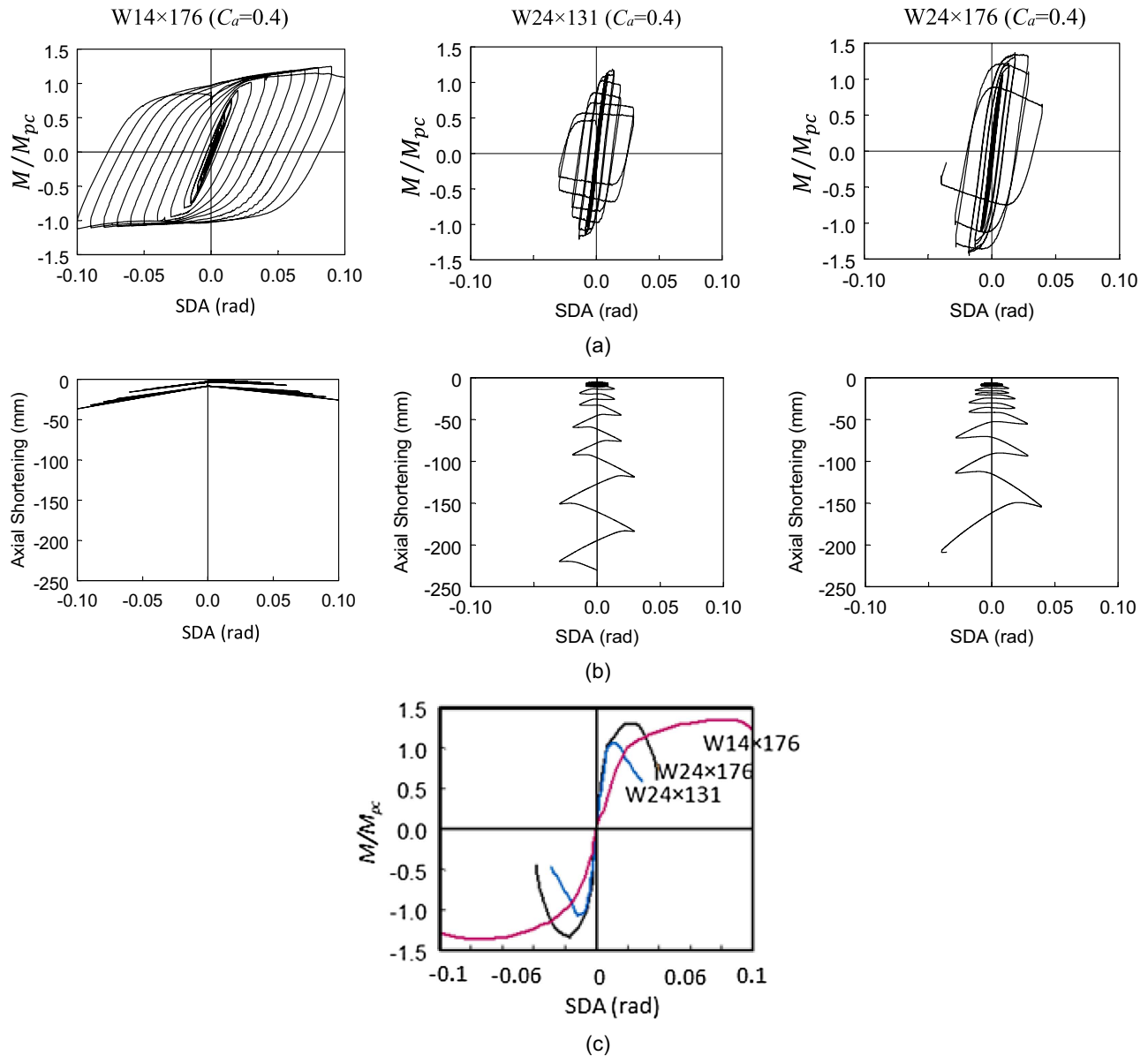
Fig. 4. Comparison of cyclic responses: (a) normalized moment versus story drift angle; (b) axial shortening versus story drift angle; and (c) backbone comparison.
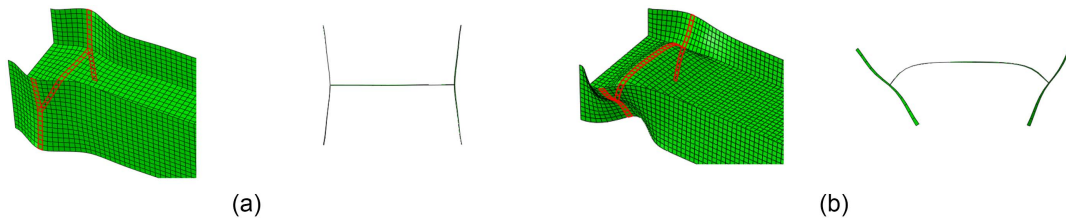

Fig. 5. Local buckling mode: (a) SFB; and (b) ALB.

bending remains in-plane without out-of-plane, global-type buckling. In the plastic hinge regions, local buckling of one flange will occur on each side of the web. The direction of buckling for each half of the same flange is the same, thus "symmetric" with respect to the web as shown in Fig. 5(a). Such buckling under monotonic loading would occur in one flange only. But both flanges would

show the same local buckling pattern under cyclic loading, although the buckling amplitude in both flanges may differ. SFB requires a relatively stocky web, i.e., low λ_w, in order to provide a sufficient rotational restraint to the flanges.

The W14 × 176 column in Fig. 6, which has $\lambda_w = 13.7$ and $C_a = 0.4$, shows such buckling mode. In the test program
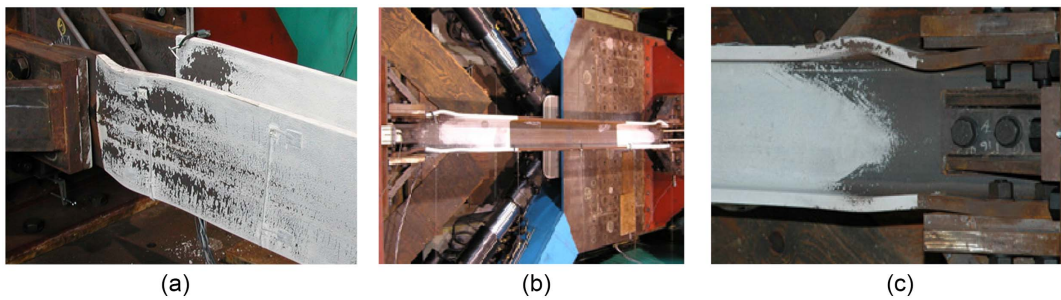
Fig. 6. SFB mode (W14 × 176, $C_a = 0.4$): (a) left end; (b) overall; and (c) right end.

(Newell and Uang 2008), it was observed that WLB either did not occur or was delayed until large drift angles. This buckling mode produces stable hysteretic response and large flexural ductility capacity. Since only flanges experienced buckling, axial shortening of the column is very limited, as shown in the first plot of Fig. 4(b).

A special case occurs when the value of flange slenderness (λ_f) is very low (say, ≤3.0). For such very stocky sections, which generally occur in built-up I-shaped, FLB ceases to occur when plastic hinges develop. No W14 or W24 rolled-shape columns tested in the NIST or AISC program fall in this special case, but numerical simulation shows this phenomenon.

Antisymmetric Local Buckling Mode

As the section slenderness ratios, especially λ_w, increase, both flange and web local buckling due to plastic hinging occur simultaneously as shown in Fig. 5(b). This buckling mode occurs mainly because the web cannot provide a sufficient rotational restraint to maintain a fix-ended boundary condition for each half of the highly compressed flange. Thus, the two half-width flanges buckle in an antisymmetric (or opposite) manner with respect to the web plane. Once the direction of loading is reversed, the buckled flange (and web) will not be straightened completely. As a result, the residual deformation serves as geometric imperfections in the next loading cycle. Since both flanges and the web have out-of-plane

deformations, the column shortens easily under the presence of an axial compression.

Fig. 7 shows examples of two W24 × 104 specimens with low and high axial loads (Specimens 3L and 3H in Table 1). Considering the northeast flange in Fig. 7(a) for example, the two half-width flanges above and below the web buckled outward and inward, respectively, and their respective apexes were not aligned in the same cross section; the apex of the outward half-flange usually is located closer to the column end. Since the web remained nearly perpendicular to the flanges at the web-flange junctions, it buckled locally in the direction that complies with the flange local buckling configuration; also see Fig. 5(b). ALB features a drastic degradation in flexural strength, which is accompanied by a significant column axial shortening. As a result, the column ductility capacity is significantly reduced when compared to that of SFB. The ductility capacity associated with this failure mode is very sensitive to the axial force level. Groups 2, 3, 13, 14, 17, and 24 specimens (W24 × 131, W24 × 104, W30 × 173, W30 × 90, W18 × 76, and W14 × 82, respectively) experienced the ALB failure mode.

Unlike SFB where the deformed column remains in the plane of bending after hinge formation, ALB would show out-of-plane movement between two end plastic hinges when local buckling becomes severe. But this out-of-plane movement is not associated with global-type LTB or FB. ALB usually starts with a one-half
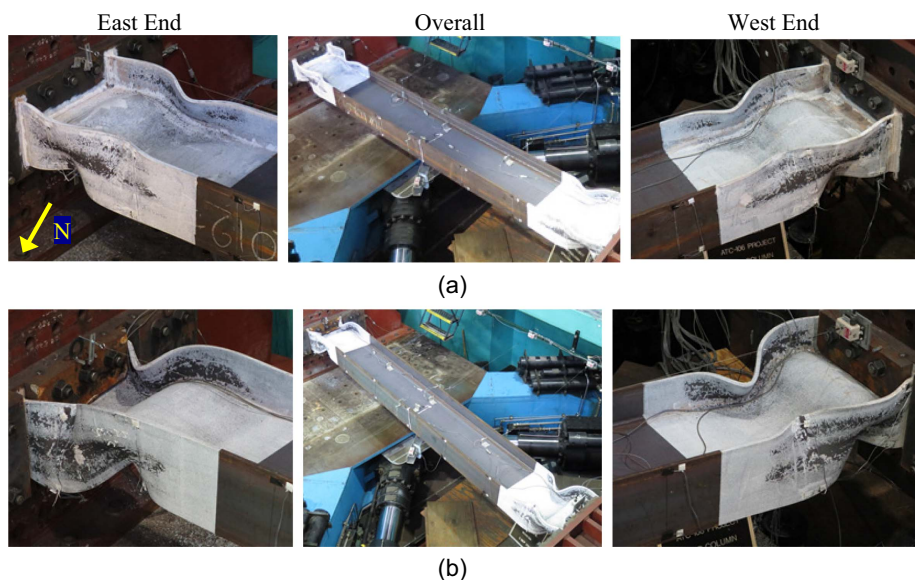

Fig. 7. ALB mode with out-of-plane movement (W24 × 104): (a) Type S (Specimen 3H); and (b) Type R (Specimen 3L).

buckle wave as shown in Fig. 5(b). At higher drift, some test specimens had the half-wave buckle extended into a full-wave buckle. In either case, the severely deformed ALB produces an out-of-plane rigid-body movement of the column segment between the member-end buckled regions; this column segment remains essentially straight and shows little torsional deformation. Although the column shows out-of-plane movement, this type of buckling should not be construed as LTB or FB. Depending on the direction of ALB at each end of the column, which in turn is dependent on the initial cross-section imperfections at the plastic hinge region, the column may appear as in either single- or reverse-curvature bending in the out of plane. That is, when the local buckling pattern at both ends of the column is the same (i.e., symmetric) with respect to the column midspan, shown as Type S mode in Fig. 7(a), both plastic hinges would result in an out-of-plane movement in the same direction (single-curvature-like out of plane bending). Conversely, a reverse-curvaturelike movement would result when the ALB patterns at both ends of the column are opposite in the out-of-plane direction, shown as Type R mode in Fig. 7(b).

Coupled Buckling Mode

It appears that this column cyclic buckling mode was not previously reported in the literature. In the NIST test program, Group 2 specimens (W24 × 131) that experienced ALB were first tested, which was then followed by Group 1 specimens (W24 × 176). Since the sections of both groups met the highly ductile requirement and the λ_f and λ_w values for Group 1 were smaller, it was thought that a similar buckling mode but with a large deformation capacity would result. Instead, an "unusual" buckling mode occurred. Such an unexpected buckling mode was

subsequently confirmed by the testing of additional specimens with different member sizes, boundary condition, and loading types in the NIST test program. Referring to Table 1, Specimens of Groups 1, 4, 11, 12, 15, 16, 22, 23, and 25 for a total of 17 specimens experienced CB. Specifically, the failure mode involved coupling between ALB and LTB.

This buckling mode may occur in either of the two scenarios, although for some specimens it is difficult to pinpoint the exact buckling sequence: (1) ALB proceeds LTB, and (2) LTB proceeds ALB. Fig. 8(a) shows an example of the former sequence with ALB proceeding LTB, Fig. 8(b) shows an example with LTB proceeding ALB. Out-of-plane global buckling about the weak-axis of these two specimens occurred in one direction. But the CB mode showing reverse curvature in the out-of-plane was also observed in several specimens; see Fig. 8(c) for an example.

Some features of CB could be observed from the flaking pattern of the whitewash paint applied at both ends of the specimens. [Specimen 27L in Fig. 8(a) was sandblasted for DIC measurements and was not whitewashed.] Fig. 7 shows that the plastic hinge length in the ALB mode is on the order of one to two times the section depth. But the flaking pattern shown in Figs. 8(b and c) indicates that the yield length is significantly longer for CB. Therefore, the concept of plastic hinge length or the lumped plastic hinge concept, strictly speaking may not apply for numerical modeling.

The flaking pattern of Specimen 1L in Fig. 8(c) is repeated in Fig. 9, but with conditions in early stages of loading also shown. Since LTB would produce warping stresses and that the brittle whitewash (or mill scale) was easier to flake off under compression, the compressive stresses or strains across the width of the flange were not uniform. Therefore, the end of the yielded zone as indicated by flaking showed a sloped pattern as shown by the dashed
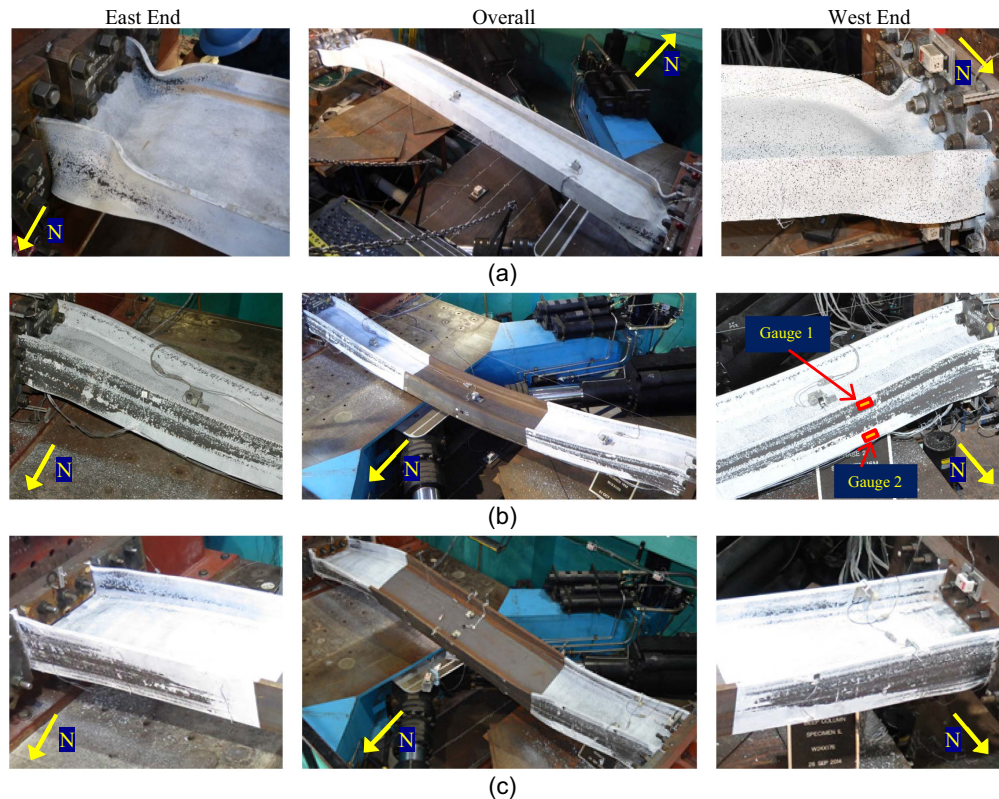

Fig. 8. Buckling sequence of CB mode: (a) single-curvature bending of W24 × 84 column with $C_a = 0.2$ (Specimen 27L); (b) single-curvature bending of W18 × 130 column with $C_a = 0.4$ (Specimen 16M); and (c) reserve-curvature bending of W24 × 176 column with $C_a = 0.2$ (Specimen 1L).
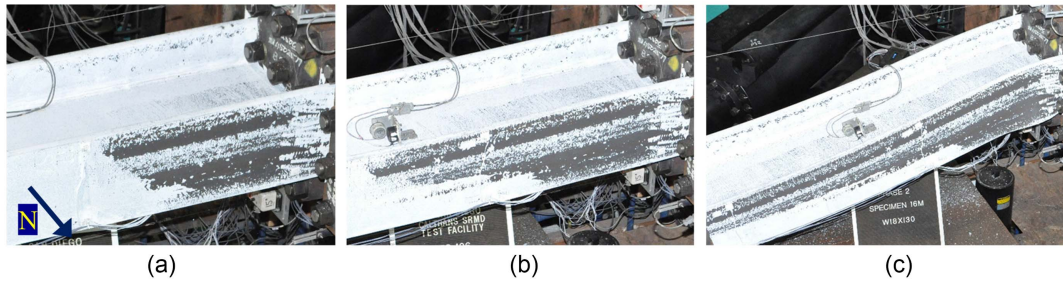
Fig. 9. Nonuniform (or sloped) flaking of whitewash at west end (Specimen 16M with W18 × 130 Section, $C_a = 0.4$): (a) $SDA = 0.015$ rad; (b) $SDA = 0.02$ rad; and (c) $SDA = 0.03$ rad.
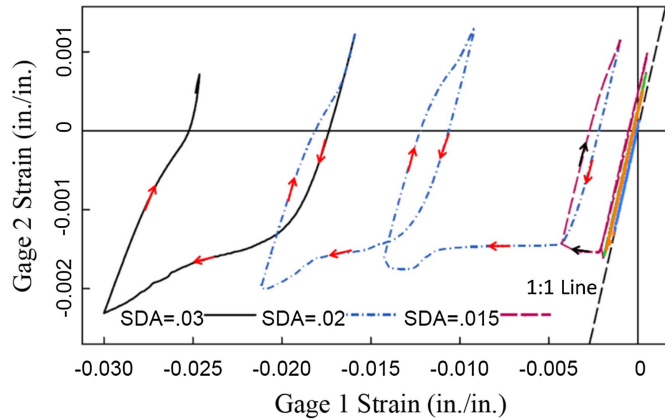

Fig. 10. Nonuniform strain profile across one flange width.

Fig. 11. LTB-induced flange local buckling (Specimen 16M): (a) northwest flange; and (b) west end.

line in Fig. 9(a). This visual feature would assist an experimentalist to identify if CB is likely to occur in the early stage of loading.

The phenomenon mentioned previously can also be confirmed by the readings of a pair of strain gages installed near the free edges of one flange of Specimen 16L [see Fig. 8(b)]. These gages were oriented in the longitudinal direction on the column. To demonstrate the effect of warping stresses, strains at both edges are plotted against each other in Fig. 10. Both strains were initially the same in sign and magnitude (data points move along the 1:1 or 45° line), indicating a uniform bending stress distribution across the flange width due to in-plane bending of the specimen. Tendency of LTB then can be observed in the plot as the data points started to deviate from the 1:1 line, which initiated at $SDA = 0.015$ rad.

Local buckling observed in the CB mode requires clarification. Refer to Fig. 11(a) for the local buckling of Specimen 16M, which exhibits one half-wave local buckle in either the top or bottom half-width flange (of the same flange), not both like the SFB or ALB pattern. Therefore, this type of flange local buckling should not be confused with the conventional local buckling as in SFB or ALB mode. Instead, it was triggered by LTB, which induces non-uniform stress distribution across the flange width because each flange bends about its strong axis (explained in the following paragraph). That is, shown in Fig. 11 is the LTB-induced flange local buckling.

CB can be further subdivided into two cases: single and reverse curvature bending modes; Figs. 8(a and b) refer to the former case, while Fig. 8(c) refers to the latter case. The terms *single curvature* and *reverse curvature* refer to the overall deformed profile. Of the 17 specimens listed in Table 1 that experienced CB, Specimens 1L, 4L, 21M-NF, 22L, and 26L-VAM deformed into reverse curvature.
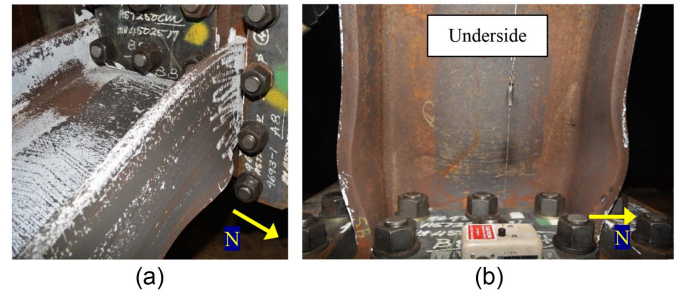
When CB develops, especially when LTB dominates the response, it was explained earlier that it is not uncommon to see symmetric-type FLB at member ends like that shown in Fig. 11. This type of local buckling may also occur at the mid-span of the column where the curvature is high. This FLB mode is triggered by significant weak-axis (i.e., out-of-plane bending) when CB develops. Therefore, this local buckling mode is not SFB presented earlier.

Interaction of Web and Flange Local Buckling

Although flanges and web in an I-shaped section will interact upon local buckling to maintain compatibility at the section level, both AISC 341 (AISC 2016a) and AISC 360 (AISC 2016b) traditionally treat FLB and WLB as independent limit states to simplify the design process (Seif and Schafer 2010). This is the case for FLB of wide-flange beams in AISC 360, with the exception that, based on Johnson (1986), the interaction between FLB and WLB of built-up I-shaped sections is explicitly considered by using a factor k_c when the flange is classified as slender, i.e., FLB in the elastic range.

Specimens 2L-P and 2L in Table 1 are two nominally identical specimens, the only difference being that 2L-P was monotonically loaded while 2P was tested cyclically. Fig. 12 shows the drastic difference in the deformed shape. For a flexural member under monotonic loading, Fig. 13(a) shows schematically the deformed cross section, where the tensile flange would help to stabilize the web. (The direction of the tilt of the compressive flange is dependent on the initial distortion or imperfection at the section level.) Under cyclic loading, however, both flanges would experience local buckling alternatively. When one flange buckles inelastically, the buckled deformation will not be restored completely under load reversal. This residual (or plastic) deformation then serves as the
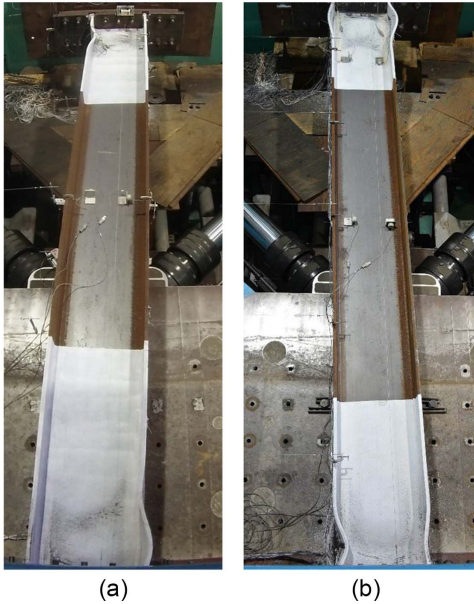
Fig. 12. Monotonic versus cyclic loading effect on local buckling mode: (a) monotonic loading (Specimen 2L-P); and (b) cyclic loading (Specimen 2L).
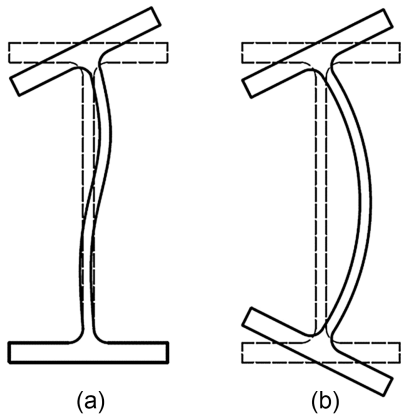

Fig. 13. Deformed cross section due to local buckling: (a) monotonic loading; and (b) cyclic loading.

initial geometric imperfection for the subsequent cycles. The resulting deformation of the cross section then becomes like that shown in Fig. 13(b).

The flange-web interaction was obvious from testing of deep wide-flange columns. Based on the results from both AISC and NIST programs, it was presented earlier that three governing buckling modes (SFB, ALB, and CB) were observed. It is desirable to develop a simple procedure to identify the governing buckling mode. In an attempt to develop such procedure, it was found that a parameter, ζ, originally derived by Han and Lee (2016) to measure the relative flexural stiffness between the flange and web, can serve as an indicator to identify the governing cyclic buckling mode when some adjustment is made to this parameter.

Monotonic Loading

Han and Lee (2016) used the mixed variational formulation to study the effect of web restraint on elastic FLB of I-shaped beams under monotonic loading. To compute the elastic buckling stress of the flange, the restraining effect was measured by using a nondimensional parameter, renamed as ζ_m herein, to express the relative flexural stiffness ratio between the flange and web:

$$\zeta_m = \frac{D_f/b}{\bar{\zeta}_m} \tag{5}$$

where $\bar{\zeta}_m$ = flexural stiffness of the web; D_f/b = flexural stiffness ratio of one-half flange; $b = b_f/2$, and D_f (flange flexural rigidity) is

$$D_f = \frac{Et_f^3}{12(1-v^2)} \tag{6}$$

The Poison ratio, v, equals 0.3. See Fig. 14(a) for the half flange width analyzed, where the dimension a represents the buckle length.

Flexural Stiffness of Web under Monotonic Loading

The derivation of the flexural stiffness of the web, $\bar{\zeta}_m$, follows. Per the procedure of Han and Lee (2016) and assuming the compressive flange buckles in a sine wave, a distributed moment, $M(x)$, develops at the flange-web junction in the buckled zone; Fig. 14(b) shows this moment applied to the full depth of the web; note the edge between the web and tension flange is modeled as simply supported (S.S.). Solve the following governing equation of the web:
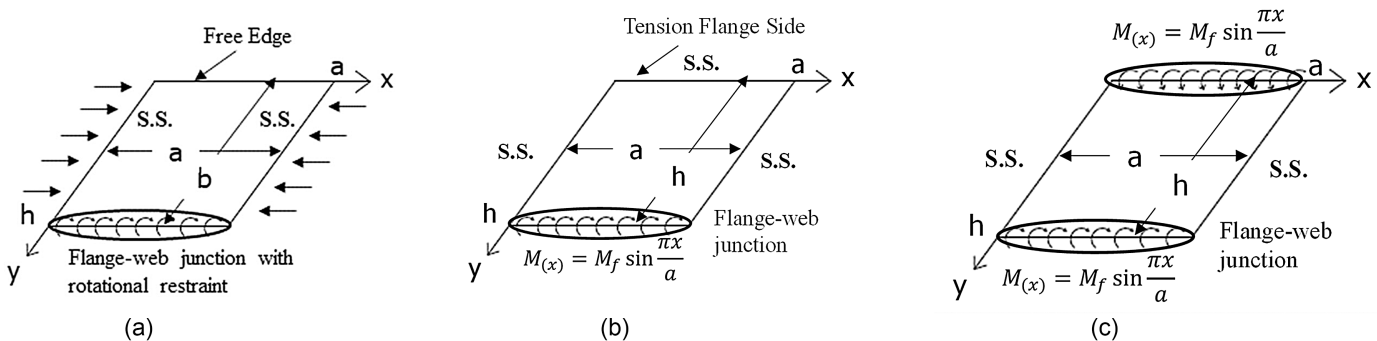

Fig. 14. Sinusoidal edge moment induced to beam web upon flange local buckling: (a) half flange model; (b) full web model for monotonic loading; and (c) full web model for cyclic loading.

$$D_w\left(\frac{\partial^4 w_w}{\partial x^4} + 2\frac{\partial^4 w_w}{\partial x^2 \partial y^2} + \frac{\partial^4 w_w}{\partial y^4}\right) = 0 \tag{7}$$

with the boundary conditions:

$$\text{for } x = 0 \text{ and } a: w_w = 0, \quad \frac{\partial^2 w_w}{\partial x^2} = 0 \tag{8a}$$

$$\text{for } y = 0: w_w = 0, \quad \frac{\partial^2 w_w}{\partial y^2} = 0 \tag{8b}$$

for $y = h$: $w_w = 0$,

$$-D_w\left[\frac{\partial^2 w_w}{\partial y^2} + \nu\frac{\partial^2 w_w}{\partial x^2}\right] = M(x) = M_f \sin\frac{\pi x}{a} \tag{8c}$$

where

$$D_w = \frac{Et_w^3}{12(1-\nu^2)} \tag{9}$$

The general solution for Eq. (7) can be written as follows (Timoshenko and Gere 1961; Salmon and Johnson 2009)

$$w_w(x,y) = \sum_{n=1}^{\infty}\left(A_n\cosh\frac{n\pi y}{a} + B_n\frac{n\pi y}{a}\sinh\frac{n\pi y}{a} + C_n\sinh\frac{n\pi y}{a} + D_n\frac{n\pi y}{a}\cosh\frac{n\pi y}{a}\right)\sin\frac{n\pi x}{a} \tag{10}$$

where the integration constants, A_n, B_n, C_n, D_n are to be determined from the boundary conditions of the web. Applying the boundary conditions in Eq. (8) gives the web transverse displacement field, w_w:

$$w_w(x,y) = \frac{1}{2\pi c \sinh(\pi c)}\left(\frac{h^2}{D_w}\right)\left[\coth(\pi c)\sinh\left(\pi c\frac{y}{h}\right)\right.$$
$$\left. - \frac{y}{h}\cosh\left(\pi c\frac{y}{h}\right)\right]M(x) \tag{11}$$

where $c = h/a$ is the aspect ratio of the buckled web. Differentiating $w_w(x; y)$ once with respect to y and then setting $y = h$, rotation $\theta(x)$ along the flange-web junction is obtained. Since the web restrains two half flanges in an I-shaped section, the web flexural stiffness per unit length, $\bar{\zeta}_m$, in Eq. (5) with respect to the half width of the flange then can be computed from $(M(x)/2)/\theta(x)$ (Han and Lee 2016). For cyclic loading, $\bar{\zeta}_m$ is renamed as $\bar{\zeta}_c$ because the boundary condition is changed. The derivations of $\bar{\zeta}_c$ and the buckle length, a, follow.

Flexural Stiffness of Web under Cyclic Loading

For local buckling under cyclic loading, the stabilizing effect provided by the tension flange in monotonic loading is overestimated. Guided by the observation from testing like that shown in Fig. 12(b), it is assumed that the buckled section bears the configuration shown in Fig. 13(b). The distributed moment, $M(x)$, is then applied at the web junctions to both flanges as shown in Fig. 14(c). The boundary conditions then need to be modified as follows:

$$\text{for } x = 0 \text{ and } a: w_w = 0, \quad \frac{\partial^2 w_w}{\partial x^2} = 0 \tag{12a}$$

for $y = 0$: $w_w = 0$,

$$D_w\left[\frac{\partial^2 w_w}{\partial y^2} + \nu\frac{\partial^2 w_w}{\partial x^2}\right] = -M(x) = -M_f\sin\frac{\pi x}{a} \tag{12b}$$

for $y = h$: $w_w = 0$,

$$D_w\left[\frac{\partial^2 w_w}{\partial y^2} + \nu\frac{\partial^2 w_w}{\partial x^2}\right] = M(x) = M_f\sin\frac{\pi x}{a} \tag{12c}$$

Repeating the same process gives the following solution for the web transverse deflection:

$$w_w(x,y) = \frac{1}{2\pi c}\left(\frac{h^2}{D_w}\right)\left[\frac{y}{h}\coth\left(\frac{\pi h}{2a}\right)\cosh\left(\frac{\pi}{c}\frac{y}{h}\right) - \frac{y}{h}\sinh\left(\frac{\pi}{c}\frac{y}{h}\right)\right.$$
$$\left. - \frac{1}{2\sinh^2\left(\frac{\pi h}{2a}\right)}\sinh\left(\frac{\pi}{c}\frac{y}{h}\right)\right]M(x) \tag{13}$$

Differentiating Eq. (13) gives the rotations at both top and bottom web-flange junction:

$$\theta(x) = \frac{\partial w_w}{\partial y}\bigg|_{y=h}$$
$$= \frac{-h/D_w}{2\pi c\sinh^2\left(\frac{\pi c}{2}\right)}\left[\frac{\pi c}{2} - \sinh\left(\frac{\pi c}{2}\right)\cosh\left(\frac{\pi c}{2}\right)\right]M(x) \tag{14}$$

The web flexural stiffness per unit length along the web-flange junction for the half flange then equals

$$\bar{\zeta}_c = \frac{1}{2}\frac{M(x)}{\theta(x)} = C_s\frac{D_w}{h} \tag{15}$$

where the coefficient C_s for cyclic loading is

$$C_s = \frac{2\left(\frac{\pi c}{2}\right)\sinh^2\left(\frac{\pi c}{2}\right)}{\sinh\left(\frac{\pi c}{2}\right)\cosh\left(\frac{\pi c}{2}\right) - \frac{\pi c}{2}} \tag{16}$$

Eq. (16) can be approximated by the following for ease of use:

$$C_s \approx 2.24 + 1.82c \tag{17}$$

Fig. 15 shows that the error is small.

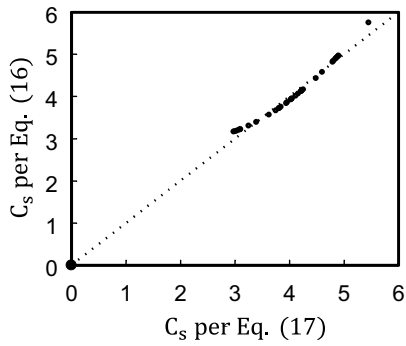**Fig. 15.** Simplification of non-dimensional web stiffness factor, C_s.

Local Buckle Length

Recall that the coefficient c in Eqs. (16) or (17) is the aspect ratio of the buckled web; thus, the buckle length, a, is needed. In the study of Han and Lee (2016) for beams under monotonic loading, a total of 35 I-shaped beams were analyzed. It was reported that the buckle lengths were more or less stable and mostly less than $3b$. Other than using a conservative value of 3 as recommended by Han and Lee, in this study a regression analysis of their data resulted in the following expression with a coefficient of correlation (R^2) of 0.96:

$$a = 1.3 b_f \sqrt{\frac{t_f}{t_w}} \tag{18}$$

Eq. (17) then can be rewritten as follows:

$$C_s = 2.24 + 1.82 \left(\frac{h}{a}\right) = 2.24 + 1.4 \left(\frac{h}{b_f}\right) \sqrt{\frac{t_w}{t_f}} \tag{19}$$

Fig. 16 shows sample local buckle length measurements. Table 2 summarizes the measured local buckle lengths of 21 deep column specimens tested in the NIST test program. Like that indicated by Lay and Galambos (1965), uncertainties existed in experimentally determining the start and end points of the buckle length. With this in mind, the measured lengths were compared with the predicted values per Eq. (18). A graphic comparison in Fig. 17 shows that Eq. (18) serves reasonably well for the prediction of local buckle length.

ζ_c and Threshold Values for Buckling Classification

Parameter ζ_m in Eq. (5) is a measure of the relative flexural stiffness between the flange and web of an I-shaped beam under monotonic loading. The modified form of Eq. (5) for cyclic loading is

$$\zeta_c = \frac{D_f/b}{\bar{\zeta}_c} = \frac{D_f h}{C_s D_w b} = \frac{1}{C_s} \left(\frac{t_f}{t_w}\right)^2 \left(\frac{\lambda_w}{\lambda_f}\right) \tag{20}$$

Substituting Eq. (19) into the preceding equation yields

$$\zeta_c = \left[\frac{\left(\frac{t_f}{t_w}\right)^2}{2.24 + 1.4 \left(\frac{h}{b_f}\right) \sqrt{\frac{t_w}{t_f}}} \right] \left(\frac{\lambda_w}{\lambda_f}\right) \tag{21}$$

Referring to the right side of Eq. (21), define A and B as follows:

$$A = \frac{\lambda_f}{\lambda_w} \tag{22}$$

$$B = \frac{\left(\frac{t_f}{t_w}\right)^2}{2.24 + 1.4 \left(\frac{h}{b_f}\right) \sqrt{\frac{t_w}{t_f}}} \tag{23}$$

such that Eq. (21) is rewritten as

$$\zeta_c = \frac{B}{A} \tag{24}$$

Variable A is a parameter that measures the relative compactness ratio between the flange and web. Variable B is a function of the relative thickness ratio between the flange and web, t_f/t_w, as well as the section aspect ratio, h/b_f. The two cross sections in Fig. 1 that have the same value of moment of inertia for strong-axis bending are used to illustrate the effect of the preceding three ratios. Table 3 shows that the value of ζ_c for the deep W27 section is 2.72 times that for the shallow W14 section.

Values of A and B for the NIST specimens in Table 2 that were tested with a fixed-fixed boundary condition and constant axial compression were computed (see Table 4). In addition, twelve shallow columns (specimens with sections W14 × 370, W14 × 233, W14 × 176, W14 × 132) from the AISC test program (Newell and Uang 2008) that experienced the SFB mode were also included in the analysis. Fig. 18 shows the distribution of these data in the $A − B$ domain; for each specimen, the observed buckling mode is also shown. It is observed that two straight lines can be drawn to separate the data with three distinct buckling modes. Since the slope of each straight line corresponds to the ζ_c value per Eq. (24), two thresholds ζ_c values based on the calibration of the test data are 2.0 and 4.0. That is, the governing cyclic buckling mode can be predicted as follows:

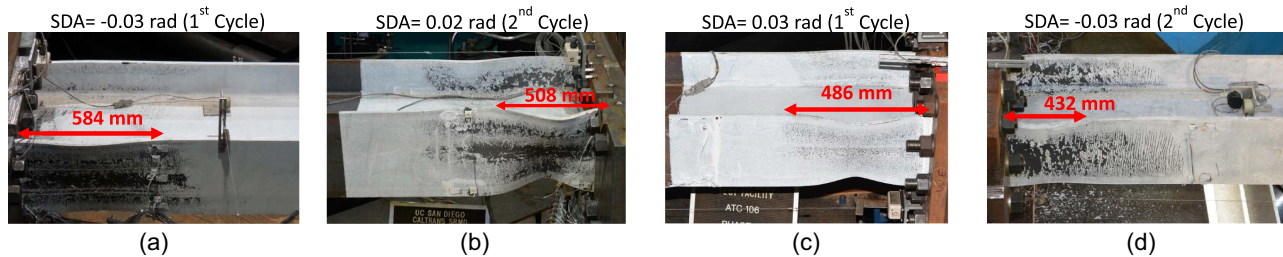1. Symmetric flange buckling (SFB):

$$\zeta_c < 0.2 \tag{25a}$$

Fig. 16. Measured buckle length: (a) specimen 2L (W24 × 131); (b) specimen 3L (W24 × 104); (c) specimen 17L (W18 × 76); and (d) specimen 24L (W14 × 82).

Table 2. Measured versus calculated buckle lengths

Group No.	Section	Specimen	Buckle length (mm) Measured	Buckle length (mm) Eq. (18)
2	W24 × 131	2L	584	574
		2M	559	574
		2H	559	574
3	W24 × 104	3L	508	552
		3M	610	552
		3H	635	552
13	W30 × 173	13M	711	683
14	W30 × 90	14L	445	429
17	W18 × 76	17L	502	486
24	W14 × 82	24L	432	450
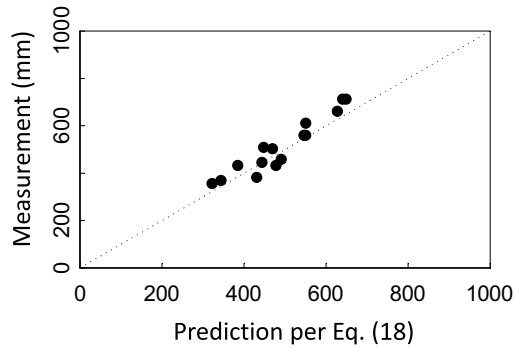
Fig. 17. Comparison of local buckle lengths.

Table 3. Parameter comparison of two sections in Fig. 1

Shape	h/b_f	λ_f/λ_w	t_f/t_w	A	B	ζ_c
W14 × 605	0.66	0.48	1.60	0.48	0.84	1.77
W27 × 258	1.67	0.17	1.81	0.17	0.80	4.82

2. Anti-symmetric local buckling (ALB):

$$2.0 \leq \zeta_c < 4.0 \tag{25b}$$

3. Coupled buckling (CB):

$$\zeta_c \geq 4.0 \tag{25c}$$
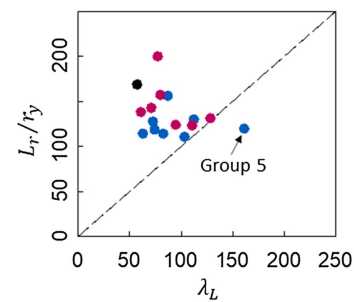
Limitation of Proposed Classification Procedure

AISC 341 does not limit the member slenderness ratio, λ_L in Eq. (1c) for first-story columns in SMF design. The λ_L values for all the NIST specimens considered in this study are listed in Table 1. Note that Group 5 specimens, which, failed by elastic LTB without hinging, had the highest λ_L value (= 161.2). According to AISC 360, the limiting unbraced length for a flexural member beyond with elastic LTB will occur is

$$L_r = 1.95 r_{ts} \frac{E}{0.7F_y} \sqrt{\frac{Jc}{S_x h_0} + \sqrt{\left(\frac{Jc}{S_x h_0}\right)^2 + 6.76\left(\frac{0.7F_y}{E}\right)^2}}$$

$$\tag{26}$$

See AISC 360 for the definition of individual terms. By using the measured F_y for the flanges, the L_r/r_y ratios for all specimens are also provided in Table 1. Plotting all data in the λ_L versus L_r/r_y domain, Fig. 19 explains why Group 5 specimens failed in elastic

Table 4. Threshold ζ values for NIST specimens

Group No.	Shape	h/b_f	λ_f/λ_w	t_f/t_w	A	B	ζ_c
1	W24 × 176	1.75	0.17	1.79	0.17	0.78	4.68
2	W24 × 131	1.75	0.19	1.59	0.19	0.60	3.20
3	W24 × 104	1.77	0.20	1.50	0.20	0.53	2.68
4	W24 × 84	2.50	0.13	1.64	0.13	0.54	4.23
5	W24 × 55	3.22	0.13	1.28	0.13	0.26	2.06
12	W30 × 261	1.86	0.16	1.77	0.16	0.75	4.69
13	W30 × 173	1.88	0.17	1.63	0.17	0.62	3.59
14	W30 × 90	2.72	0.15	1.30	0.15	0.30	2.04
15	W18 × 192	1.47	0.20	1.82	0.20	0.88	4.51
16	W18 × 130	1.51	0.19	1.79	0.19	0.84	4.32
17	W18 × 76	1.53	0.21	1.60	0.21	0.65	3.03
22	W30 × 148	2.70	0.11	1.82	0.11	0.65	6.12
23	W18 × 60	2.22	0.14	1.67	0.14	0.60	4.29
24	W14 × 82	1.25	0.26	1.68	0.26	0.78	2.96
25	W14 × 53	1.56	0.20	1.78	0.20	0.82	4.15
26	W14 × 132	0.86	0.40	1.60	0.40	0.80	1.98
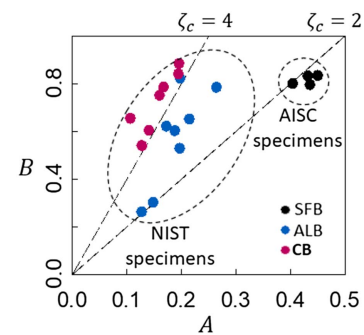
Fig. 18. Threshold ζ values for buckling classification.

Fig. 19. Global slenderness ratio of the NIST specimens versus global slenderness limits.

LTB. The length of all other NIST specimens that experienced either ALB or CB did not exceed L_r. Therefore, the proposed buckling classification procedure can be applied to column members where the member length (i.e., first-story height) does not exceed L_r.

Summary and Conclusions

Wide-flange columns are widely used in steel braced frames and special moment frames for seismic resistance. While shallow and stocky shapes are common for braced frames, design engineers prefer to use deep shapes for the more flexible special moment frames in recent years because these shapes, for their larger strong-axis

moment of inertia, are more efficient to meet the stringent story drift limits in building codes. Although columns in a special moment frame are required to meet the strong column-weak beam requirement in order to remain essentially elastic, plastic hinging at the column base is still expected.

Column buckling under cyclic loading is much more complicated than that under monotonic loading. Based on a recent NIST-sponsored research project on deep column response under axial compression and cyclic drifts (Chansuk et al. 2021), it was observed that these columns would experience two types of buckling modes, one involving in-plane plastic hinging and the other one also including lateral-torsional buckling in the out of plane. These buckling modes are different from the local buckling pattern of shallow and stocky columns observed from an AISC-sponsored column research project (Newell and Uang 2008). Several buckling modes of wide-flange columns have been observed not only from these two projects but also by other researchers, yet no consistent classification on the cyclic buckling modes has been established. Sometimes, the same buckling mode may be interpreted by different researchers in different ways, which causes confusion.

The classification proposed in this paper includes symmetric flange buckling (SFB), antisymmetric local buckling (ALB), and coupled buckling (CB). The first one mainly occurs in columns with shallow and stocky sections, while the remaining two mainly occur in columns with deep sections. Subsets of each buckling mode are also presented.

Building upon a prior study on monotonic loading (Han and Lee 2016) and after considering the effect of cyclic loading, a parameter, ζ_c in Eq. (24) that measures the relative rotational restraint the web provides to the flanges, can be used to separate three buckling modes observed from both the NIST and AISC test programs. After calibrating this parameter against the test data, this criterion is presented in Eq. (25).

Data Availability Statement

Some or all data, models, or code that support the findings of this study are available from the corresponding author upon reasonable request. This includes the test data.

Acknowledgments

References

AISC. 2016a. *Seismic provisions for structural steel buildings*. ANSI/AISC 341-16. Chicago: AISC.

AISC. 2016b. *Specification for structural steel buildings*. ANSI/AISC 360-16. Chicago: AISC.

ASCE. 2016. *Minimum design loads and associated criteria for buildings and other structures*. ASCE/SEI 7-16. Reston, VA: ASCE.

ASCE. 2017. *Seismic evaluation and rehabilitation of existing buildings*. ASCE/SEI 41-17. Reston, VA: ASCE.

Chansuk, P., G. Ozkula, C.-M. Uang, and J. L. Harris III. 2021. *Seismic behavior and design of deep, slender wide-flange structural steel beam-columns*. NIST Technical Note 2169. Gaithersburg, MD: NIST.

Cravero, J., A. Elkady, and D. G. Lignos. 2020. "Experimental evaluation and numerical modeling of wide-flange steel columns subjected to constant and variable axial load coupled with lateral drift demands." *J. Struct. Eng.* 146 (3): 04019222. https://doi.org/10.1061/(ASCE)ST.1943-541X.0002499.

Elkady, A., and D. G. Lignos. 2012. "Dynamic stability of deep slender steel columns as part of special MRSF designed in seismic regions: Finite element modelling." In *Proc., 1st Int. Conf. on Performance-Based and Life-Cycle Structural Engineering*. Hong Kong: Hong Kong Polytechnic Univ.

Elkady, A., and D. G. Lignos. 2015. "Analytical investigation of the cyclic behavior and plastic hinge formation in deep wide-flange steel beam-columns." *Bull. Earthquake Eng.* 13 (4): 1097–1118. https://doi.org/10.1007/s10518-014-9640-y.

Elkady, A., and D. G. Lignos. 2018. "Full-scale testing of deep wide-flange steel columns under multi-axis cyclic loading: Loading sequence, boundary effects and out-of-plane brace force demands." *J. Struct. Eng.* 144 (2): 04017189. https://doi.org/10.1061/(ASCE)ST.1943-541X.0001937.

Fogarty, J., and S. El-Tawil. 2016. "Collapse resistance of steel columns under combined axial and lateral loading." *J. Struct. Eng.* 142 (1): 04015091. https://doi.org/10.1061/(ASCE)ST.1943-541X.0001350.

Fogarty, J., T. Y. Wu, and S. El-Tawil. 2017. "Collapse response and design of deep steel columns subjected to lateral displacement." *J. Struct. Eng.* 143 (9): 2017. https://doi.org/10.1061/(ASCE)ST.1943-541X.0001848.

Han, K.-H., and C.-H. Lee. 2016. "Elastic flange local buckling of I-shaped beams considering effect of web restraint." *Thin-Walled Struct.* 105 (Aug): 101–111. https://doi.org/10.1016/j.tws.2016.04.001.

Johnson, D. L. 1986. "An investigation into the interaction of flanges and webs in wide flange shapes." In *Proc., Annual Technical Session and Meeting*, 397–405. Bethlehem, PA: Structural Stability Research Council.

Lay, M. G., and T. V. Galambos. 1965. "Inelastic steel beams under uniform moment." *J. Struct. Div.* 91 (6): 67–93. https://doi.org/10.1061/JSDEAG.0001370.

Newell, J. D., and C.-M. Uang. 2008. "Cyclic behaviour of steel wide-flange columns subjected to large drift." *J. Struct. Eng.* 134 (8): 1334–1342. https://doi.org/10.1061/(ASCE)0733-9445(2008)134:8(1334).

NIST. 2011. *Research plan for the study of seismic behavior and design of deep, slender, wide-flange structural steel-beam-column members*. NIST-GCR-11-917-13. Gaithersburg, MD: NIST.

Ozkula, G., J. Harris, and C. M. Uang. 2017. "Observations from cyclic tests on deep, wide-flange beam-columns." *Eng. J.* 54 (1): 45–61.

Ozkula, G., C. M. Uang, and J. Harris. 2021. "Development of enhanced seismic compactness requirements for webs in wide-flange steel columns." *J. Struct. Eng.* 147 (7): 1–12. https://doi.org/10.1061/(ASCE)ST.1943-541X.0003036.

Ozkula, G., and C.-M. Uang. 2015. *Seismic behavior and design of deep, slender wide-flange structural steel beam-column: Phase 1 testing*. Rep. No. SSRP-15/06. San Diego: Univ. of California.

Salmon, C., and J. Johnson. 2009. *Steel structures: Design and behavior, emphasizing load and resistance factor design*. 4th ed. New York: HarperCollins College Publishers.

Seif, M., and B. W. Schafer. 2010. "Local buckling of structural steel shapes." *J. Constr. Steel Res.* 66 (10): 1232–1247. https://doi.org/10.1016/j.jcsr.2010.03.015.

Timoshenko, S. P., and J. M. Gere. 1961. *Theory of elastic stability*. New York: Dover Publications.

Wu, T. Y., S. El-Tawil, and J. McCormick. 2018. "Highly ductile limits for deep steel columns." *J. Struct. Eng.* 144 (4): 04018016. https://doi.org/10.1061/(ASCE)ST.1943-541X.0002002.

Zargar, S., R. A. Medina, and E. Miranda. 2014. "Cyclic behavior of deep steel columns subjected to large deformation demands and high axial loads." In *Proc., 10th US National Conf. on Earthquake Engineering*. Oakland, CA: EERI.